JOURNAL OF combinatorial CHEMISTRY

Article

Automated Electrochemical Synthesis and Photoelectrochemical Characterization of Zn$_{1-x}$Co$_x$O Thin Films for Solar Hydrogen Production

Thomas F. Jaramillo, Sung-Hyeon Baeck, Alan Kleiman-Shwarsctein, Kyoung-Shin Choi, Galen D. Stucky, and Eric W. McFarland

J. Comb. Chem., **2005**, 7 (2), 264-271• DOI: 10.1021/cc049864x • Publication Date (Web): 29 December 2004

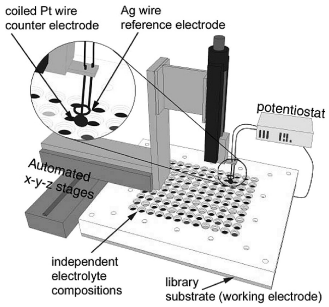

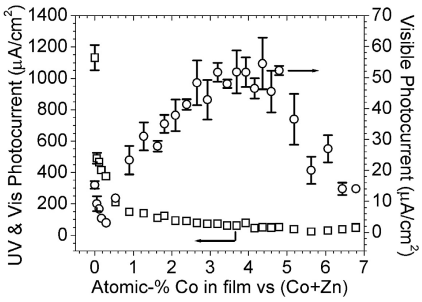

More About This Article

Additional resources and features associated with this article are available within the HTML version:

- Supporting Information
- Links to the 5 articles that cite this article, as of the time of this article download
- Access to high resolution figures
- Links to articles and content related to this article
- Copyright permission to reproduce figures and/or text from this article

View the Full Text HTML

Automated Electrochemical Synthesis and Photoelectrochemical Characterization of $Zn_{1-x}Co_xO$ Thin Films for Solar Hydrogen Production

Thomas F. Jaramillo,[†] Sung-Hyeon Baeck,[‡] Alan Kleiman-Shwarsctein,[†] Kyoung-Shin Choi,[§] Galen D. Stucky,[||] and Eric W. McFarland*,[†]

Department of Chemical Engineering, University of California, Santa Barbara, California 93106-5080, Department of Chemical Engineering, Inha University, Incheon, Korea 402-751, Department of Chemistry, Purdue University, 560 Oval Drive, West Lafayette, Indiana 47907-2084, and Department of Chemistry and Biochemistry, University of California, Santa Barbara, California 93106

Received August 12, 2004

High-throughput electrochemical methods have been developed for the investigation of $Zn_{1-x}Co_xO$ films for photoelectrochemical hydrogen production from water. A library of 120 samples containing 27 different compositions ($0 \leq x \leq 0.068$) was synthesized by automated serial electrochemical deposition. High-throughput photoelectrochemical screening revealed improved solar hydrogen production for the cobalt-doped films, with $Zn_{0.956}Co_{0.044}O$ exhibiting a 4-fold improvement over pure ZnO with no external bias. Flat-band potential, bias-dependent photocurrent, and action spectra were also measured automatically with the high-throughput screening system. The 200-nm-thick films were subsequently characterized by numerous techniques, including SEM, XRD, XPS, and UV−vis, which show that the depositions are well-controlled. Zn/Co stoichiometry in the films was controlled by the ratio of the Zn and Co precursors in each deposition bath. All films exhibited the wurtzite structure typical of pure ZnO, and the Co^{2+} appears to substitute Zn^{2+}, forming a single-phase solid solution. Band gaps of the solid solutions were systematically lower than the 3.2-eV band gap typical of ZnO.

1. Introduction

Efficient hydrogen production by photoelectrochemical water-splitting from sunlight is considered a "holy grail" of chemistry.[1] Since the groundbreaking work of Fujishima and Honda in 1972, hydrogen synthesis by photoelectrolysis as a clean and renewable energy source has stimulated the imagination of many researchers.[2] Despite decades of research, today's best photoelectrocatalytic systems suffer from limitations that prevent their incorporation into the commercial energy market: efficient material systems are typically expensive or unstable, whereas inexpensive and robust alternatives do not have adequate efficiency.[3] The majority of work has been on substituted and doped TiO_2 hosts or relatively expensive multiple gap photoelectrodes.[3,4] In this report, we examine ZnO as a potential single gap host oxide and use automated synthesis and screening techniques to explore cobalt doping as a means of improving its properties for photoelectrochemical hydrogen production.

The photoelectrochemical activity of ZnO has been studied extensively for decades.[5−11] It has been well-established that ZnO photocatalysts have two primary limitations: (1) poor solar spectrum photon absorption (due to a wide band gap of 3.2 eV) and (2) photocorrosion in electrolytes. It has been shown that at high pH, photocorrosion can be reduced, and improved solar photon absorption has been achieved by adding various transition-metal cations as substituents or dopants into the ZnO host lattice.[8,9,12−15] Bahadur and Rao prepared cobalt-doped ZnO by spray pyrolysis and explored materials with five different Zn/Co ratios (from 0 to 5 mol %).[14] They found that 2 mol % cobalt-doping was the "optimal" composition for photoactivity in acetonitrile. More recently, Hirano and Kozuka synthesized cobalt-doped ZnO by sol−gel dip-coating and investigated seven different Zn/Co ratios (from 0 to 67 mol %) and found that 5 mol % was optimal in an aqueous (pH 9.18) solution.[15] Both works explored few compositions, and neither group reported statistical variations for identically prepared samples.

To rapidly explore the effects on the functional properties of materials with diverse compositional variations, a methodology of experimentation was introduced by Joseph Hanak in the late 1960s.[16] Hanak's concept of improving the efficiency of material science by combining rapid synthesis with high-throughput screening has evolved into what is now called high-throughput or combinatorial material science, and numerous recent works concerning the high-throughput synthesis and screening of solid-state materials have appeared. Although an exhaustive exploration of all possible ZnO-based mixed-oxide compounds is unachievable, high-throughput techniques applied to binary, ternary, and quaternary zinc oxides *may* greatly expedite the investigation and discovery

[†] Department of Chemical Engineering, University of California, Santa Barbara.
[‡] Inha University.
[§] Purdue University.
[||] Department of Chemistry and Biochemistry, University of California, Santa Barbara.

10.1021/cc049864x CCC: $30.25
Published on Web 12/29/2004

of improved materials. We have developed systems for high-throughput evaluation of metal oxides and herein report the investigation of $Zn_{1-x}Co_xO$ in a library of 120 samples synthesized by a novel automated electrochemical deposition method and screened for photoelectrochemical hydrogen production using an automated photoelectrochemical cell.

Several recent publications have reported the development of combinatorial methods to investigate mixed zinc oxide materials for diverse applications, including magnetic materials (spintronics), phosphors, transparent conductors, and catalysis.[17−20] Most researchers utilized vacuum deposition techniques (pulsed laser deposition, sputtering, etc.) for material synthesis. Recently, our group has developed electrochemical methods for the controlled, automated synthesis of metal oxides, including WO_3 and MoO_3 as well as true mixed metal oxides.[21−23] In general, there are few reports in the literature of mixed-oxide electrodeposition, almost certainly because of the complex nature of the electrodeposition process, as compared to predictable materials synthesized by vacuum deposition techniques or sol−gel.[24]

Electrochemical synthesis of materials can be advantageous because it is low-cost, high speed, and relatively easy to scale up. Additionally, the synthesized material forms a direct electrical contact with the substrate (without which deposition would never take place). This inherent characteristic is unique to electrodeposited films and for our particular area of interest can be a considerable advantage over thin films produced by dip-coating, spin-coating, inkjet printing, or vapor deposition.

In this report, we address the following questions: (1) Can automated methods of electrochemistry be used to synthesize libraries of mixed ZnO/CoO films as solid solutions? (2) Is it possible to control the stoichiometry of electrochemically deposited $Zn_{1-x}Co_xO$ films? (3) What is the crystal structure of the $Zn_{1-x}Co_xO$ films? (4) How do the optical and photoelectrochemical properties of $Zn_{1-x}Co_xO$ films compare to those of pure ZnO? (5) What is the optimal $Zn_{1-x}Co_xO$ stoichiometry for photoelectrochemical hydrogen production?

2. Results and Discussion

2.1. Library Design and Synthesis. A 120-member $Zn_{1-x}Co_xO$ ($0.000 \leq x \leq 0.068$) library was designed with compositional diversity achieved through variation of deposition electrolytes across the library (Figure 1). The library consists of 27 distinct ratios of Zn/Co with four replicates at each composition for statistical analysis (108 samples). The remaining 12 samples (all located in the first row) were used for temperature equilibration and voltage calibration of the counter and reference electrodes during ZnO synthesis.

The automated electrochemical deposition system developed for automated $Zn_{1-x}Co_xO$ library synthesis is shown schematically in Figure 2. The system produces a 10 × 12 array of thin-film samples on a 163 mm × 138 mm substrate (typically fluorine-doped tin oxide (FTO)/glass, TEC-15, Pilkington). Samples are 9 mm in diameter and spaced 3.5 mm apart. Details on a similar, early-generation electrodeposition system have been published.[21] Independent electrochemical cells (120) are formed by sealing a perforated

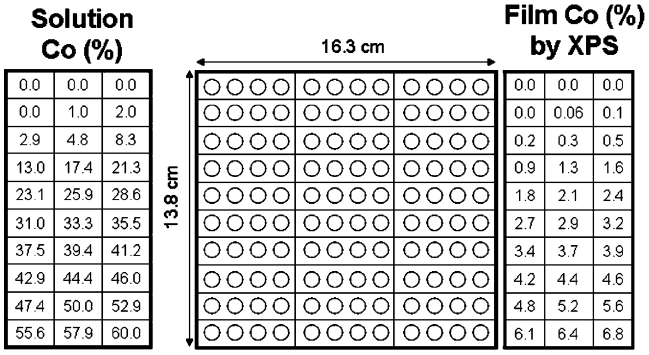

Solution Co (%)		
0.0	0.0	0.0
0.0	1.0	2.0
2.9	4.8	8.3
13.0	17.4	21.3
23.1	25.9	28.6
31.0	33.3	35.5
37.5	39.4	41.2
42.9	44.4	46.0
47.4	50.0	52.9
55.6	57.9	60.0

Film Co (%) by XPS		
0.0	0.0	0.0
0.0	0.06	0.1
0.2	0.3	0.5
0.9	1.3	1.6
1.8	2.1	2.4
2.7	2.9	3.2
3.4	3.7	3.9
4.2	4.4	4.6
4.8	5.2	5.6
6.1	6.4	6.8

Figure 1. Library design for $Zn_{1-x}Co_xO$ materials. 120 materials: 27 different material compositions were explored, with four replicates each. The table to the left shows the variation in $Co(NO_3)_2$ concentration (vs $Co(NO_3)_2 + ZnCl_2$) in the deposition baths across the library. The table to the right shows the resulting concentration of cobalt in the films, determined by XPS.

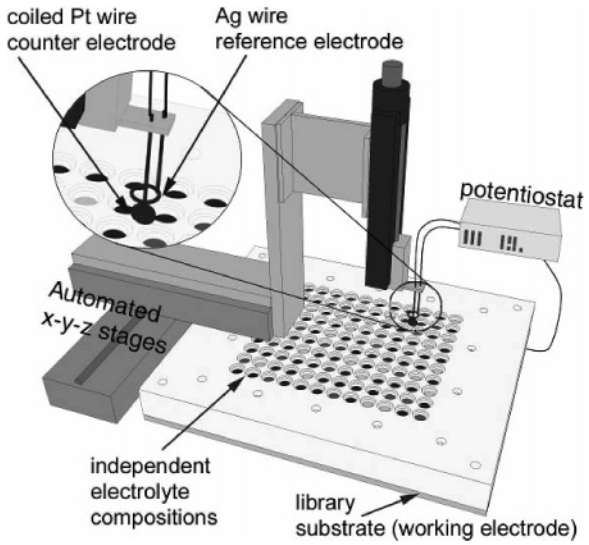

Figure 2. Automated rapid serial electrochemical deposition system for a 10 × 12 array of thin films. The library substrate is sealed (by O-rings) underneath a perforated Teflon block, and each of the 120 cells is filled with a unique electrolyte composition.

Teflon block onto the substrate using independent O-rings. Each cell (1.5 mL) is manually filled with a specific electrolyte using an electronic Repeater Pro Pipetter (Eppendorf, Germany), which dispenses the liquid with <5-μL imprecision (manufacturer specification). An automated set of $x-y-z$ stages positions and submerges a Pt wire counter electrode (wound into a flat, spiral coil) and Ag wire reference electrode into each sealed cell for rapid serial electrodeposition under computer control.

All films were transparent, and most appeared to have no color, except for those synthesized with cobalt concentrations >6 atomic %, which exhibited a beige hue. Although all films revealed a similar consistency in the middle of the circular sample, it is worth noting that films synthesized with the higher concentrations of cobalt (>3 atomic %) exhibited a dark ring at their edges. This arises from preferential cobalt or cobalt oxide deposition in the vicinity of the O-ring; solutions with greater concentrations of $Co(NO_3)_2$ yielded thicker and wider rings than those with lower concentrations. Because the conductivity of FTO is much greater than that of the electrolyte, the FTO substrate can be treated as an

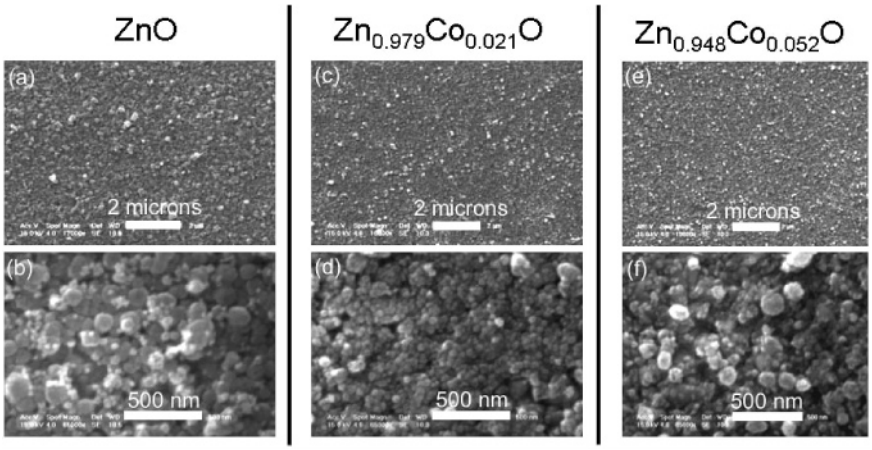

Figure 3. SEM images of three selected library members. All films exhibited a similar morphology, that of densely packed particles, roughly 20−200 nm in size and shaped spherically or as platelets.

equipotential surface. Although the working and counter electrode geometries are similar (both circular, of approximately the same area, and parallel to each another), the electric field may be enhanced at the edges due to differences in the dielectric coefficients of the solution and the O-ring/Teflon block and nonuniformity of the electric field. These effects are thought to be responsible for the preferential deposition of cobalt at the edges, but further investigation of this phenomenon is outside the scope of this manuscript, because the center (∼90%) region of each film was uniform, and it is this portion of the sample that is under investigation microscopically, spectroscopically, and photoelectrochemically.

A Sloan DekTak II profilometer was used to investigate film thickness of all library samples to ensure uniform thickness in the center region. Large spikes were observed at the edges, as expected; however, the center region measured 200 nm (± 5% min/max) for all samples, regardless of composition.

2.2. Morphology and Composition (SEM and XPS). Figure 3 shows SEM results from selected library members. All films revealed similar morphologies, despite compositional variations; films consisting of fairly dense particles, approximately spherical or platelet in shape and ranging from approximately 20 to 200 nm in diameter, were observed. The film morphologies resembled those synthesized by Gal et al.[25]

XPS was utilized for compositional analysis and to characterize the Co valence state of 10 selected films. Figure 4a shows the XPS spectrum in the Co 2p region for $Zn_{0.961}Co_{0.039}O$. This particular sample yields XPS data that well represents all Co-containing films we measured. Four broad peaks in the Co 2p region are observed, all of which are assigned to Co^{2+} on the basis of the binding energy of the Co $2p_{3/2}$ peak (781.0 eV), the energy difference between Co $2p_{1/2}$ and $2p_{3/2}$ peaks (15.9 eV), and the binding energies of the broad shake-up satellite peaks (786.0 and 802.6 eV) (Table 1).[26] Figure 4b shows XPS spectra for six selected films ranging from 0.0 to 5.2 atomic % cobalt. For all films examined, the peaks demonstrate nearly identical shape, position, and fwhm, indicating that Co^{2+} is the predominant species in all films, regardless of stoichiometry. No zero valence Co and only a small fraction of Co^{3+} was observed

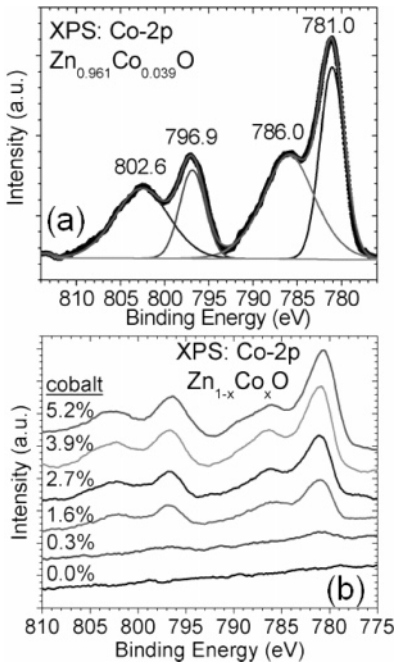

Figure 4. XPS of the Co 2p region for selected library samples. (a) Deconvolution of a typical spectrum for these materials, as represented by $Zn_{0.961}Co_{0.039}O$. (b) Multiple spectra for different concentrations of cobalt.

Table 1. Assignment of Co 2p X-ray Photoelectron Binding Energies, in Agreement with Literature Values for Co^{2+} [26]

spectral region	binding energy (fwhm)	assignment
Co $2p_{3/2}$	781.0 eV (3.2)	Co^{2+} multiplet spitting
	786.0 eV (6.8)	Co^{2+} shake-up satellite
Co $2p_{1/2}$	796.9 eV (3.4)	Co^{2+} multiplet spitting
	802.6 eV (7.2)	Co^{2+} shake-up satellite

for samples with cobalt concentrations of >5.0%. Figure 5a illustrates the correlation between Co atomic % in the film and in the deposition solution, which was fitted using a second-order polynomial, yielding an R^2 value of 0.998. Zn/Co stoichiometry for all library films was interpolated on the basis of this analysis, and it was found that the concentration of cobalt in the films ranged from 0.0 to 6.8%, $Zn_{1-x}Co_xO$ ($0.000 \leq x \leq 0.068$). Figure 1 specifies film stoichiometry for all films within the library.

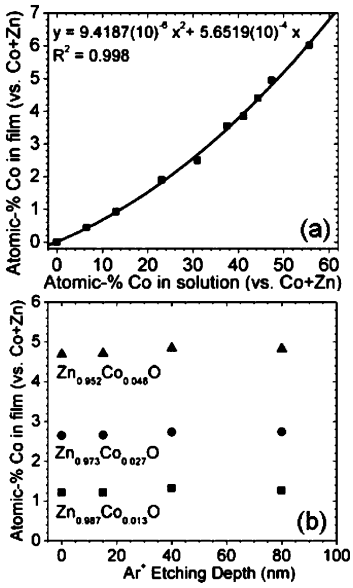

Figure 5. $Zn_{1-x}Co_xO$ stoichiometry by XPS. (a) Comparison of cobalt content in the film vs cobalt in the deposition bath. (b) Ar^+ etching was employed to investigate stoichiometry as a function of depth; film compositions were quite homogeneous.

Because XPS is only surface-sensitive, ion etching was employed to examine stoichiometry as a function of depth within the films. Because cobalt and zinc have similar atomic masses, etch rates were expected to be similar. Figure 5b illustrates the results from the etching study. The composition changes are negligible as a function of depth, indicating a homogeneous distribution of the cobalt within the ZnO host.

2.3. Crystal Structure (XRD). X-ray diffraction (XRD) was performed to investigate the crystal structure of the films. Because of the similar ionic radii of Co^{2+} and Zn^{2+}, high degrees of solubility of Co (up to 70%) have been observed within ZnO.[27] At low concentrations of cobalt (under ~20 atomic %), most researchers have observed the wurtzite structure for pure ZnO and cobalt-doped ZnO.[15,17,27] The appearance of a spinel (Co_3O_4 or $ZnCo_2O_4$) phase or rocksalt (CoO) phase seems to depend as strongly upon synthesis route, conditions, and precursors as it does on cobalt concentration and temperature. XPS results show that the cobalt concentrations of all films in the library are relatively low (<10%), and phase separation is not expected. We were unable to restrict the X-ray diffractometer source to a single library member, and thus, for XRD studies, five selected samples, three of which represented the higher end of cobalt fraction, were resynthesized on independent substrates for XRD measurements. Figure 6 shows these results in comparison to the expected peak positions for wurtzite ZnO and spinel Co_3O_4. All five spectra match the wurtzite phase of ZnO, with no evidence of other phases.

XPS and XRD measurements reveal that these films form solid solutions of ZnO and CoO. Once this control of the composition and structure had been achieved, the investigation of optical and photoelectrochemical experiments could then be undertaken.

2.4. Optical Properties. The optical properties of photoelectrochemical materials are of utmost importance because they dictate the number of photons absorbed by the system, perhaps the most critical factor in determining efficiency.

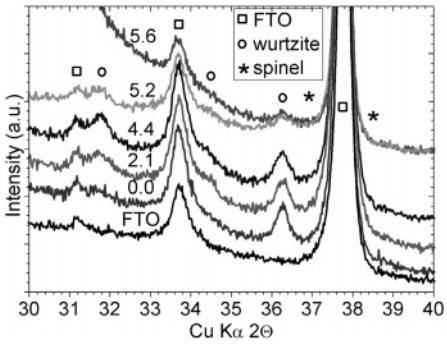

Figure 6. XRD of selected compositions of $Zn_{1-x}Co_xO$; mol % Co in the film is marked above each diffraction pattern. Regardless of composition, all materials exhibited a wurtzite crystalline phase, almost identical to that of pure ZnO.

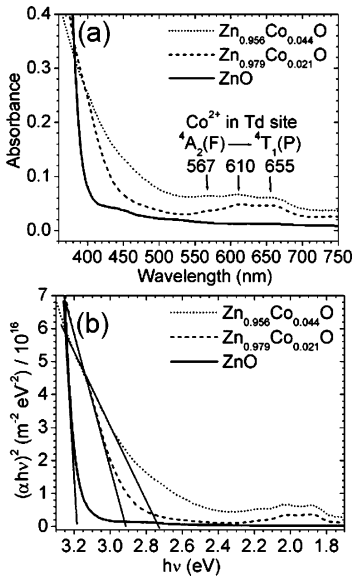

Figure 7. UV−vis spectroscopy of selected $Zn_{1-x}Co_xO$ samples. (a) Cobalt-doping gives rise to increased absorption of visible light by means of characteristic Co^{2+} $d-d$ transitions at 567, 610, and 655 nm, as well as a shifted absorption edge that implies a change in band gap. (b) Band gap calculations for direct-gap semiconductors reveal that the band gap of ZnO is systematically lowered with increasing cobalt.

UV−vis spectroscopy was performed on all samples to observe changes in optical properties as a function of material composition. Three representative spectra are shown in Figure 7a, measured from films 1 μm thick. All cobalt-doped samples exhibit strong absorption bands between 540 and 680 nm. The peaks at 567 (2.2 eV), 610 (2.0 eV), and 655 nm (1.9 eV) are assigned to $^4A_2(F) \rightarrow {}^4T_1(P)$ transitions within tetrahedrally coordinated Co^{2+}, in agreement with previous work.[12−14] This is consistent with our XPS and XRD data, all of which support a model in which a divalent cobalt ion, Co^{2+}, substitutes Zn^{2+} within the tetrahedral sites of the hcp O^{2-} lattice (the wurtzite structure). It is important to note that these $d-d$ transitions are energetically sufficient to split water ($\Delta G = 1.23$ eV), and so they are expected to play a role in photoelectrochemical hydrogen production as long as (1) the absolute energies of the electron−hole pair match well with water redox potentials and (2) the charge carriers are sufficiently mobile to avoid recombination and reach the electrode surfaces.

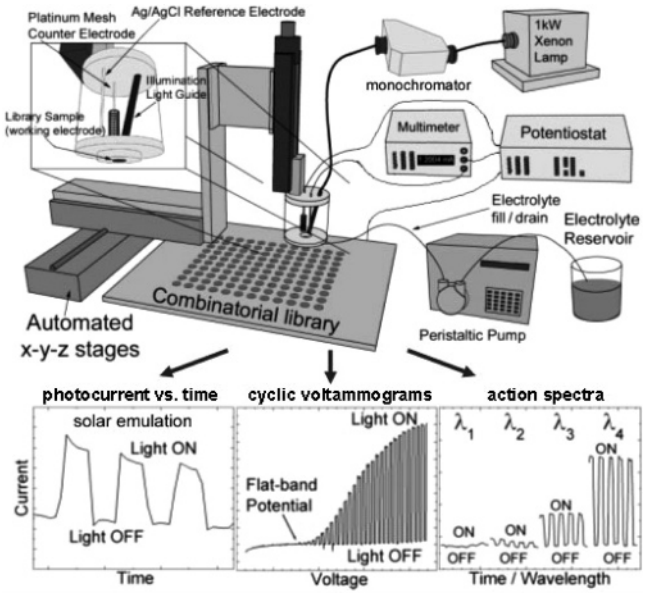

Figure 8. Automated high-throughput photoelectrochemical screening. A uniquely designed photoelectrochemical probe is stepped across the library from sample to sample for various automated measurements under computer control.

With increasing cobalt concentration, the absorption edge shifts to longer wavelengths, indicating a change in the effective band gap (E_g) energy. To determine the E_g value for a direct band gap semiconductor, the absorbance coefficient (α) was calculated from absorbance data and then a plot of $(\alpha h\nu)^2$ vs $h\nu$ was constructed, Figure 7b; a linear fit to the data gives E_g as the x intercept.[28,29] Pure ZnO intercepts at 3.20 eV, in excellent agreement with the literature, whereas the E_g values for $Zn_{0.979}Co_{0.021}O$ and $Zn_{0.956}Co_{0.044}O$ were found to be 2.90 and 2.75 eV, respectively.[29] A systematic reduction in E_g is observed for the cobalt-doped samples. The deviation from linearity observed for the $Zn_{0.956}Co_{0.044}O$ sample in Figure 7b is attributed to lower crystallinity (as observed by XRD for the higher cobalt-doped samples).

2.5. High-Throughput Photoelectrochemical Screening. For high-throughput photoelectrochemical screening, in which material performance is evaluated, we designed and constructed a scanning photoelectrochemical probe (Figure 8). The detailed construction and operation is described elsewhere.[21] In short, the probe is affixed to an automated $x-y-z$ stage and steps from sample-to-sample across the library. An inert O-ring at the bottom (which is slightly smaller than the O-rings used for synthesis) forms a seal as the cell is moved down on each sample and an automated pump fills the probe with 50 mL of solution from a reservoir. An optical fiber targets chopped illumination directly upon the sample. A Pt mesh counter electrode and a Ag/AgCl reference electrode are used in obtaining photoelectrochemical data from the sample. An automated filter wheel can move a UV cutoff filter (<400 nm) into the beam path to simulate solar radiation, while an electronic shutter chops the light source up to 40 Hz.

2.5.1. Short-Circuit Photocurrent. The photogenerated current (photocurrent) measured under short-circuit conditions is the primary screening technique used to identify materials active for photoelectrochemical hydrogen production. Photocurrent (which is calculated by the subtraction of the dark current from the current obtained during illumination) is a direct, quantitative measure of redox activity generated by absorbed photons and, in this particular case, a measure of H_2 production off the Pt counter electrode. Upon illumination, electron−hole pairs are generated within the bulk of $Zn_{1-x}Co_xO$, and because of the materials' *n*-type nature, an electric field is produced within the semiconductor that directs holes toward the electrode−electrolyte interface while electrons move toward the back contact (FTO) and through the external circuit to the Pt-mesh counter electrode. The hydrogen evolution reaction (HER) predominates because platinum is a well-known catalyst for this reaction; the reduction of dissolved O_2 to O^{2-} can be neglected because the solution was purged with N_2 for 30 min prior to experiment and was continuously purged throughout the course of the experiment. Oxygen evolution on the $Zn_{1-x}Co_xO$ surface arises from water oxidation as well as photoanodic corrosion.

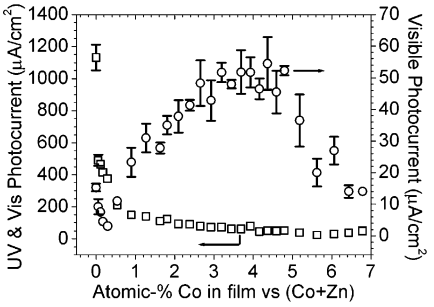

Figure 9. Photocurrent in 0.2 M KNO_3 as a function of $Zn_{1-x}Co_xO$ composition without the application of an external bias. Two forms of illumination were used, UV−vis (left axis, black squares, 1.77 W/cm^2) and vis only (right axis, blue circles, 1.50 W/cm^2), which simulates solar radiation.

The $Zn_{1-x}Co_xO$ library was examined for short-circuit photocurrent at zero bias: all 120 samples were screened in ~4 h. The filter wheel automatically inserted a UV cutoff filter to first record photocurrent under visible illumination and then removed the filter from the beam path for the measurement of photocurrent under full spectrum (UV−vis) illumination. Photocurrent measurements under the two illumination conditions are shown in Figure 9. With broad spectrum, UV−vis illumination, a trend in photocurrent with increased Co is observed: pure ZnO shows the greatest photocurrent (1130 ± 80 μA/cm^2), and this value drops sharply with increasing Co %, even at very low concentrations. The UV−vis photocurrent asymptotically approaches 60 μA/cm^2 at higher concentrations of cobalt. Although the cobalt-doped samples absorb more visible light than pure ZnO, because of the presence of UV light in this case, all samples absorb a significant fraction of the incident radiation. Unfortunately, cobalt acts as a trapping or recombination center for electrons and holes, and under UV−vis illumination, this process dominates increased visible band absorption, and we observe a decrease in the overall broad spectrum photoactivity with increasing cobalt.

The trends observed in the visible spectrum photocurrent are more encouraging. Under visible-band illumination, pure ZnO exhibits 15 ± 1 μA/cm^2 of photocurrent, and with very low concentrations of Co ($Zn_{1-x}Co_xO$, $x \leq 0.003$) the

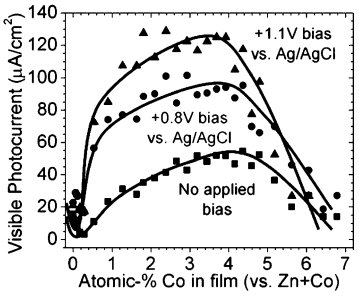

Figure 10. Photocurrent of $Zn_{1-x}Co_xO$ materials under vis-only illumination with the aid of an external bias.

photocurrent falls to 3 ± 0.5 μA/cm^2 from recombination and defect trapping; there is insufficient additional photon absorption to offset the decrease in conductivity. With further increases in the concentration of Co, the $Zn_{1-x}Co_xO$ photocurrent steadily increases until reaching a maximum of 55 ± 8 μA/cm^2 at $x = 0.044$, a 4-fold improvement over pure ZnO; the increased photon absorption produces more carriers than are trapped or recombined until a maximum is achieved at 4.4% Co. Materials with cobalt concentrations >4.4% exhibited decreased performance with increasing cobalt until reaching a visible photocurrent of 14 ± 2 μA/cm^2, a value similar to that of pure ZnO, for $x = 0.064$ and 0.068.

2.5.2. Bias-Dependent Photocurrent. Cyclic voltammograms for all library samples were measured with the high-throughput photoelectrochemical screening system under chopped illumination. A positive, applied bias is expected to increase photocurrent generation of these *n*-type materials as the Fermi levels of the two electrodes move in appropriate directions to facilitate water splitting and assist charge separation. For cost-effective photoelectrochemical hydrogen production, it is preferable to avoid utilizing an applied bias. If the external bias is small (about several tenths of a volt), however, the gains from improved performance could possibly outweigh the cost (in terms of energy added) of applying the bias. Figure 10 shows the photocurrent measured for all library samples under visible illumination (i.e., with the UV filter in place) at +0.8 and +1.1 V vs Ag/AgCl. The data from Figure 9 (photocurrent with no applied bias) are also shown for comparison. As expected, a larger external bias results in greater capture of photon-generated charge carriers and an increased redox rate. The same general trend in performance is observed for all three conditions as a function of composition. The +1.1-V bias improves the photogenerated current by a factor of ~2.5, as compared to the zero-applied bias case.

2.5.3. Action Spectrum/IPCE. To study photoelectrochemical performance as a function of incident wavelength, the high-throughput photoelectrochemical screening system was used in conjunction with a monochromator to obtain action spectra of library samples for incident radiation between 370 and 700 nm. The incident photon conversion to electron efficiency (IPCE) was calculated by measuring the radiation intensity at each wavelength and then using the following equation:

$$\mathrm{IPCE}(\%) = \frac{(1240)(i_{\mathrm{photocurrent}}\ \mu\mathrm{A/cm^2})}{(\lambda\ \mathrm{nm})(j_{\mathrm{photons}}\ \mu\mathrm{W/cm^2})} \times 100\%$$

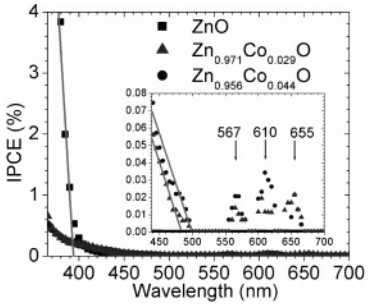

Figure 11. IPCE of selected $Zn_{1-x}Co_xO$ samples. Increased cobalt loading shifts the edge of photocurrent to longer wavelengths, consistent with a decrease in the band gap energy. The characteristic Co^{2+} $d-d$ transitions observed in UV−vis spectroscopy are also responsible for increased visible light photoelectrochemical activity.

Figure 11 illustrates the results from several selected samples on the library. Not surprisingly, pure ZnO showed high photoactivity with illumination <400 nm, consistent with a ZnO band gap of ~3.2 eV, as determined earlier by UV−vis spectroscopy. The cobalt-doped materials show very little photocurrent in this region compared to ZnO, an expected result given the difference in performance under UV illumination, as observed in Figure 9. The inset of Figure 11 magnifies the 450−700-nm spectral region. Whereas pure ZnO shows no measurable photocurrent, the cobalt-doped samples exhibit strong photoactivity. Increased photocurrent in this region is derived from two sources: first, a decrease in the band gap of these $Zn_{1-x}Co_xO$ materials, which shifts the absorption edge to longer wavelengths; and second, from characteristic $d-d$ transitions at 567, 610, and 655 nm observed for tetrahedrally coordinated Co^{2+}. Both of these features appeared in the UV−vis spectroscopy of Figure 7, and it is clear that the extra visible photon absorptions of $Zn_{1-x}Co_xO$ materials directly led to greater photoelectrochemistry. Overall quantum efficiencies and IPCE values, under solar-simulated radiation, are presented in Table 2.

2.5.4. Flat-Band Potential. The onset voltage at which photocurrent is first observed in the cyclic voltammograms approximates the flat-band potential of the material, which is a measure of the band-bending of the semiconductor system in contact with the electrolyte.[12,13,30] Because these materials are *n*-type semiconductors (largely a result from oxygen vacancies and Zn^{1+} interstitials) with large carrier concentrations, the flat band potential and conduction band energy are nearly identical.[5,12,15] For all compositions of $Zn_{1-x}Co_xO$ within the library, the flat-band potential was found to be -0.21 ± 0.05 V vs Ag/AgCl, with no systematic trends observed (Figure 12). This observation suggests that the conduction band edge of ZnO is marginally affected by cobalt substitution into the lattice. This result is in agreement with the work of Fichou et al. as well as Schoenmakers et al.[11,12] The UV−vis spectroscopy data above indicate that the incorporation of cobalt reduces the band gap of ZnO (Figure 7), and if the conduction band position remains unchanged, as suggested from the flat-band measurement, then it is the valence band that is effectively raised to a higher energy level due to the introduction of cobalt into the bulk.[12] This is desirable, since the energetics of the ZnO conduction band are appropriate for hydrogen evolution, whereas the valence band is excessively deep for water oxidation.

Table 2. Photoelectrochemical Results for 200-nm-Thick ZnO and $Zn_{0.956}Co_{0.044}O$ Films under Illumination by a Xe Lamp with a UV Cutoff Filter ($\lambda > 400$ nm) in Place (1.5 W/cm^2)

sample	photocurrent	absorptance	quantum efficiency	IPCE
ZnO	15 μA/cm^2	0.1−0.5%	0.2−1.0%	0.0027%
$Zn_{0.956}Co_{0.044}O$	55 μA/cm^2	1.0−1.8%	0.6−1.0%	0.010%
			2.5−5.8% ($\lambda = 610$ nm)	0.04% ($\lambda = 610$ nm)

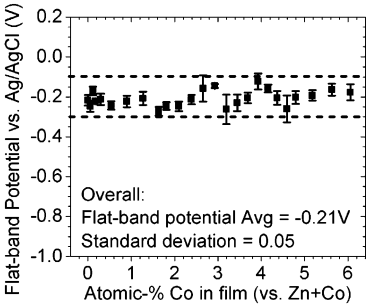

Figure 12. Flat-band potential of $Zn_{1-x}Co_xO$ films, as determined by the onset of photocurrent during cyclic voltammograms in 0.2 M KNO_3 (pH 6.7).

The absorption bands in the 1.8−2.2-eV range are attributed to a Co^{2+} defect band whose ground-state electrons lie in the middle of the ZnO band gap.[12−15] The action spectrum above shows that these electrons have sufficient energetics and mobility for photoelectrochemical hydrogen production.

3. Conclusions

Automated electrochemical synthesis and screening of mixed zinc oxides in a library of 120 $Zn_{1-x}Co_xO$ ($0.000 \leq x \leq 0.068$) films was used for the investigation of improved materials for photoelectrochemical hydrogen production. Variations in electrolytes allowed for diversity in film composition. Selected materials were thoroughly characterized by traditional techniques, including XRD, SEM, XPS, and UV−vis. All films exhibited the wurtzite structure, and Co^{2+} was observed as a substitutional dopant. Moderate concentrations of cobalt (∼2−5 mol %) led to a large increase in photocurrent from visible-band illumination, with $Zn_{0.956}Co_{0.044}O$ (effective $E_g = 2.75$ eV) exhibiting four times the photocurrent of pure ZnO. The action spectra collected by high-throughput screening closely resembled trends observed in UV−vis spectroscopy, which supports the role of Co^{2+} augmenting photoelectrochemical activity through increased visible photon absorption, primarily through a significant decrease in band gap (despite relatively low concentrations of cobalt) and secondarily from $d-d$ absorptions in the region of 540−680 nm attributed to Co^{2+}. Using the high-throughput screening system, flat-band potentials were measured and found to change negligibly as a function of composition, which indicates that the conduction band lies at approximately the same energy, regardless of $Zn_{1-x}Co_xO$ composition. Given the change in the absorption edge for these materials (as observed by UV−vis), the valence band energy is effectively raised with increasing cobalt concentrations.

Experimental Section

Library Synthesis. The synthesis rate was 2 min per sample, and the library was synthesized in ∼4 h. All solutions contained 100 mM $ZnCl_2$ and 60 mM $LiNO_3$ solvated in dimethyl sulfoxide (DMSO), a modified synthetic route adopted from Gal et al.[25] $Co(NO_3)_2 \cdot 6H_2O$ concentrations ranged from 0 to 150 mM across the library. All reagents were ACS grade and obtained from Acros. Each sample was deposited for 60 s at 105 °C and at −1.15 V vs the Ag wire pseudo reference electrode (approximately −1.0 V vs a standard Ag/AgCl reference). These particular conditions were chosen because they (1) produced films with the stoichiometry of interest and (2) deposited films rapidly, an important requirement for high-speed serial synthesis. Immediately after synthesis, the library was rinsed with copious amounts of DI water and then calcined in air at 500 °C for 8 h.

Sample Characterization. An FEI Co. XL30 environmental scanning electron microscope (ESEM) was used in high-vacuum mode to examine film morphologies. X-ray photoelectron spectroscopy was conducted with a Kratos Axis Ultra using a monochromated Al-Kα source (1486.6 eV) for excitation and an eight-channel detector. This is a commercial instrument, not an automated high-throughput tool of our construction, which took measurements one location at a time for ∼1.5 h at each spot. Base pressure was $\sim 5 \times 10^{-10}$ Torr, and spectra were calibrated to C-1s at 285.0 eV. Zn/Co ratios were determined by ratios of the peak areas for Zn $2p_{3/2}$ and Co $2p_{3/2}$ photoelectron emission, after normalizing with Scofield sensitivity factors. Ion etching was conducted at an Ar partial pressure of 10^{-7} Torr with an applied 4 kV and 1.6 μA, resulting in a ∼5 nm/min etch rate. XRD was conducted with a Phillips XPERT powder diffractometer using Cu-Kα radiation and a CNRS position sensitive detector. UV−vis spectroscopy was conducted in a diffuse reflectance configuration using a SpectraLab 7.5-cm-diameter integrating sphere. A 1-kW lamp (SpectraPhysics) was used for incident radiation and an Ocean Optics S2000 spectrometer for detection.

For photoelectrochemical characterization, N_2-purged 0.2 M KNO_3 (aq, pH 6.7) was used as the electrolyte, and a 1-kW Xe (SpectraPhysics) was used for illumination. A chopping frequency of 1 Hz was used for the measurement of short-circuit photocurrent with and without an applied bias. For cyclic voltammograms, 3 Hz was used. An International Light IL1705 radiometer was used to measure the incident radiation with (1.50 W/cm^2) and without (1.77 W/cm^2) the UV cutoff filter in place. The cyclic voltammograms consisted of two scans measured from −0.8 to +1.2 V vs a Ag/AgCl reference electrode at a rate of 200 mV/s using a PAR EG&G 273A potentiostat; the first scan was measured while the sample was illuminated with the UV cutoff filter in place, and the subsequent scan, under the full spectrum of the Xe lamp. A SpectraPhysics Cornerstone 260 monochromator was used with a 1200 l/mm grating and 6.32-mm

slits to achieve 20-nm band-pass (fwhm) light at 5-nm increments from 700 to 370 nm.

Acknowledgment. Major funding was provided by the Hydrogen Program of the Department of Energy (Grant No. DER-FC36-01G011092). Support in part was provided by the MRSEC Program of the National Science Foundation under Award No. DMR00-80034. T.F.J. thanks the GEM Consortium, the Rohm & Haas Company, and Rockwell for fellowships. The authors thank Dr. Tom Mates, Mr. Shahid Shaikh, and Mr. Michael Obradovitch for technical assistance.

References and Notes

(1) Bard, A. J.; Whitesides, G. M.; Zare, R. N.; McLafferty, F. W. *Acc. Chem. Res.* **1995**, *28*, 91.
(2) Fujishima, A.; Honda, K. *Nature* **1972**, *238*, 37−38.
(3) Bak, T.; Nowotny, J.; Rekas, M.; Sorrell, C. C. *Int. J. Hydrogen Energy* **2002**, *27*, 991−1022.
(4) Tryk, D. A.; Fujishima, A.; Honda, K. *Electrochim. Acta* **2000**, *45*, 2363−2376.
(5) Morrison, S. R.; Freund, T. *J. Chem. Phys.* **1967**, *47*, 1543−1551.
(6) Gomes, W. P.; Freund, T.; Morrison, S. R. *Surf. Sci.* **1968**, *13*, 201−208.
(7) Micka, K.; Gerischer, H. *Electroanal. Chem. Interface Electrochem.* **1972**, *38*, 397−402.
(8) Inoue, T.; Fujishima, A.; Honda, K. *B. Chem. Soc. Jpn.* **1979**, *52*, 3217−3220.
(9) Kikuchi, E.; Itoh, K.; Katoh, T.; Fujishima, A. *B. Chem. Soc. Jpn.* **1989**, *62*, 2789−2792.
(10) Hotchandani, S.; Kamat, P. *J. Electrochem. Soc.* **1992**, *139*, 1630−1634.
(11) Schoenmakers, G. H.; Vanmaekelbergh, D.; Kelly, J. J. *J. Phys. Chem.* **1996**, *100*, 3215−3220.
(12) Fichou, D.; Pouliquen, J.; Kossanyi, J.; Jakani, M.; Campet, G.; Claverie, J. *J. Electroanal. Chem.* **1985**, *188*, 167−187.
(13) Jakani, M.; Campet, M.; Claverie, J.; Fichou, D.; Pouliquen, J.; Kossanyi, J. *J. Solid State Chem.* **1985**, *56*, 269−277.
(14) Bahadur, L.; Rao, T. N. *Sol. Energy Mater. Sol. Cells* **1992**, *27*, 347−360.
(15) Hirano, T.; Kozuka, H. *J. Mater. Sci.* **2003**, *38*, 4203−4210.
(16) Hanak, J. J. *J. Mater. Sci.* **1970**, *5*, 964−971.
(17) Jin, Z.; Fukumura, T.; Kawasaki, M.; Ando, K.; Saito, H.; Sekiguchi, T.; Yoo, Y. Z.; Murakami, M.; Matsumoto, Y.; Hasegawa, T.; Koinuma, H. *Appl. Phys. Lett.* **2001**, *78*, 3824−3826.
(18) Perkins, J. D.; del Cueto, J. A.; Alleman, J. L.; Warmsingh, C.; Keyes, B. M.; Gedvilas, L. M.; Parilla, P. A.; To, B.; Readey, D. W.; Ginley, D. S. *Thin Solid Films* **2002**, *411*, 152−160.
(19) Mordkovich, V.; Hayashi, H.; Haemori, M.; Fukumura, T.; Kawasaki, M. *Adv. Funct. Mater.* **2003**, 13, 519−524.
(20) Kiener, C.; Kurtz, M.; Wilmer, H.; Hoffmann, C.; Schmidt, H.-W.; Grunwaldt, J.-D.; Muhler, M.; Schüth, F. *J. Catal.* **2003**, *216*, 110−119.
(21) Jaramillo, T. F.; Baeck, S.-H.; Kleiman-Shwarsctein, A.; McFarland, E. W. *Macromol. Rapid Commun.* **2004**, *25*, 297−301.
(22) Baeck, S.-H.; Jaramillo, T. F.; Jeong, D. H.; McFarland, E. W. *Chem. Commun.* **2004**, *4*, 390−391.
(23) Baeck, S.-H.; Jaramillo, T. F.; Brändli, C.; McFarland, E. W. *J. Comb. Chem.* **2002**, *6*, 563−568.
(24) Pauporté, Th.; Goux, A.; Kahn-Harari, A.; de Tacconi, N.; Chenthamarakshan, C. R.; Rajeshwar, K.; Lincot, D. *J. Phys. Chem. Solids* **2003**, *64*, 1737−1742.
(25) Gal, D.; Hodes, G.; Lincot, D.; Schock, H.-W. *Thin Solid Films* **2000**, *361*, 79−83.
(26) Chuang, T. J.; Brundle, C. R.; Rice, D. W. *Surf. Sci.* **1976**, *59*, 413−429.
(27) Jayaram, V.; Rajkumar, J.; Sirisha Rani, B. *J. Am. Ceram. Soc.* **1999**, *82*, 473−476.
(28) Keis, K.; Roos, A. *Opt. Mater.* **2002**, *20*, 35−42.
(29) Memming, R. *Semiconductor Electrochemistry*; Wiley-VCH Verlag GmbH: Weinheim, Germany, 2001.
(30) Peraldo Bicelli, L.; Pedeferri, P.; Razzini, G. *Int. J. Hydrogen Energy* **1986**, *11*, 647−651.

CC049864X